The Determination of the Spatial Distribution of Indigenous Lipid Biomarkers in an Immature Jurassic Sediment using ToF-SIMS

Pasterski, M. J.[1*], Lorenz, M. [2], Ievlev, A. V.[2], Wickramasinghe, R. C.[3], Hanley, L.[3], Kenig, F.[1*]

1. Department of Earth and Environmental Sciences, University of Illinois Chicago, Chicago, Illinois, USA.
2. Center for Nanophase Materials Sciences, Oak Ridge National Laboratory, Tennessee, USA.
3. Department of Chemistry, University of Illinois Chicago, Chicago, Illinois, USA.

*Corresponding authors: Michael J. Pasterski (mpaste3@uic.edu) and Fabien Kenig (fkenig@uic.edu)

Abstract

The ability to detect and map lipids, including potential lipid biomarkers, within a sedimentary matrix using mass spectrometry (MS) imaging may be critical to determine if potential lipids detected in samples returned from Mars are indigenous to Mars or are contaminants. Here, we use gas chromatography – mass spectrometry (GC-MS) and time of flight – secondary ion mass spectrometry (ToF-SIMS) datasets collected from an organic-rich, thermally immature Jurassic geologic sample to constrain MS imaging analysis of indigenous lipid biomarkers in geologic samples. GC-MS data shows that the extractable fractions are dominated by C_{27}-C_{30} steranes and sterenes as well as isorenieratene derivatives. ToF-SIMS spectra from organic matter-rich laminae contain a strong, spatially restricted signal for ions *m/z* 370.3, *m/z* 372.3, and *m/z* 386.3, which we assign to C_{27} sterenes, cholestane (C_{27}), and 4- or 24-methyl steranes (C_{28}), respectively, as well as characteristic fragment ions of isorenieratene derivatives including *m/z* 133.1, *m/z* 171.1 and *m/z* 237.1. We observed individual steroid spatial heterogeneity at the scale of 10's to 100's of microns. The fine-scale heterogeneity observed implies that indigenous lipid biomarkers concentrated within specific regions may be detectable via ToF-SIMS in samples with even low amounts of organic carbon, including in samples returned from Mars.

Word count: 5515 (excluding section 2. Materials and Methods)

Keywords: Organic geochemistry, mass spectrometry imaging, ToF-SIMS, GC-MS, lipid biomarkers, organic molecular biosignatures, geology, Mars sample return

1. Introduction

In a geological context, lipid biomarkers are organic molecules found in the geosphere that retain enough chemical structural information to be attributable to a defined biological source (Peters and Moldowan, 1993). Biomarker analyses are useful for understanding the chemical and biological evolution of life on Earth. In an astrobiological context, lipid biomarkers and lipid biomarker patterns are both included in the ensemble of organic molecular biosignatures that could provide evidence for the existence of extraterrestrial life (Neveu *et al.,* 2018). The utility of any lipid biomarker depends on the biomarker's origin. Lipid biomarkers can be: i) indigenous or syn-depositional; ii) non-indigenous organics incorporated into a host rock during fluid migration including petroleum migration and hydrothermal activity; or iii) contaminants incorporated during sample collection, storage, or analysis.

Lipid biomarkers are usually extracted from crushed rocks or sediments using organic solvents. The resulting solvent extracts can typically be separated into subfractions of different polarity using preparative methods like column chromatography prior to analysis with chromatographic instruments coupled to a mass spectrometer. This traditional approach is well suited for biomarker analysis because it results in the resolution of complex mixtures often present in sedimentary organic matter. However, the initial sample crushing obliterates the spatial relationship between organic matter and the inorganic components. Such a loss of information is problematic because one efficient way to determine the origin of a biomarker is to determine its spatial distribution within a host rock (Fig. 1; Brocks, 2011; Medina Ferrer *et al.,* 2018). Mass spectrometry imaging (MSI), the mapping of organic compounds based on the distribution of a characteristic mass to charge ratio (*m/z*), is one effective technique to study the spatial relationship between biomarkers and the other components of a host rock.

The first step associated with MS imaging is the desorption of material from the surface of a sample using a focused high-energy source such as a laser or a liquid metal ion source (Fig. 1). The material desorbed from the surface of the sample is either ionized during desorption or ionized subsequently in an additional postionization step (Hanley *et al.,* 2019). After ionization, the ions are detected by a mass spectrometer. Multiple analyses performed across the surface of a

sample can be stitched together to form a raster with each pixel corresponding to a mass spectrum, a plot of the intensity vs. mass to charge ratio (*m/z*) of each ion detected by the MS. The intensity of each ion abundance or any combination of ion abundances can then be mapped, showing the spatial distribution of the ions in the analyzed area. Current MS imaging analytical techniques include time-of-flight secondary ion mass spectrometry (ToF-SIMS; Thiel and Sjövall, 2011; Gilmore, 2013; Ivarsson *et al.,* 2013; Massonnet and Hereem, 2019), femtosecond – laser desorption postionization – mass spectrometry (fs-LDPI-MS; Hanley *et al.,* 2019), laser desorption ionization – mass spectrometry (LDI-MS; Lauzon *et al.,* 2015; Li *et al.,* 2017), matrix assisted laser desorption ionization mass spectrometry (MALDI; Li *et al.,* 1994; Lee *et al.,* 2019), and many other custom-built and hybrid systems (Wörmer *et al.,* 2014; Paine et al. 2017; Wörmer *et al.,* 2020).

The Mars 2020 Perseverance rover is currently collecting and caching cores of rock and sediment samples in Jezero crater (Ehlman *et al.,* 2008; Cloutis *et al.,* 2016; Goudge *et al.,* 2018; Beaty *et al.,* 2019) for a future Mars Sample Return (MSR; Beaty *et al.,* 2019; Farley *et al.,* 2020). Detection of indigenous molecular organic biomarkers within the sedimentary matrix of MSR samples may be critical to confirm their Martian origin. ToF-SIMS is capable of detecting organic compounds, including biomarkers, within natural samples including geologic samples and dehydrated biologic samples such as microbial mats (Thiel and Sjövall, 2011).

Previous ToF-SIMS studies of lipid molecular biomarkers include those of individual compounds and mixtures of compounds diluted in solvents and drop-cast on cleaned silicon wafers prior to analysis. Targets analytes of previous ToF-SIMS analysis have included individual hopanes and steranes (Steele *et al.,* 2001; Sjövall *et al.,* 2008; Siljeström *et al.,* 2009), individual lipids and lipid mixtures including hopanes, *n*-alkanes, polycylic aromatic compounds (PAHs), CHN compounds and isoprenoids (Toporski and Steele, 2004), individual glycerolipids (Heim *et al.,* 2009), individual cyclic lipids including multiple individual cholestanes, hopanes and hopenes, as well as α-tocopherol, β,β – carotene, and chlorophyll *a* (Leefman *et al.,* 2013b), and multiple individual alkanes, wax esters and glycerolipids (Siljeström *et al.,* 2017). In natural material, organic compounds have been analyzed in microbial stringers and lipid extracts collected from a modern hot springs (Siljeström *et al.,* 2017), cryosections and lipid extracts

from modern microbial mats (Thiel *et al.,* 2007; Heim *et al.,* 2009; Leefmann *et al.,* 2013a), oil-bearing fluid inclusions in hydrothermal fluorite and calcite veins (Siljeström *et al.,* 2010) and within a Proterozoic sandstone (Siljeström *et al.,* 2013), crude oil and crude oil fractions (Sjövall *et al.,* 2008; Siljeström *et al.,* 2009) and on isolated kerogen (Sjövall *et al.,* 2021). In planetary sciences, ToF-SIMS has been performed on meteorites (Stephan, 2001; Stephan *et al.,* 2003; Noun *et al.,* 2019) and on cometary particles (Stephan *et al.,* 2008). Most relevant to this analysis, Thiel et al. (2014) utilized ToF-SIMS in conjunction with GC-MS to compare fatty acids and *n*-alkanes extracted from modern whale bones to kerogenous material extracted from and within ancient whale bones.

Here, we utilize ToF-SIMS on an ancient sediment sample relevant to astrobiology. To the best of our knowledge, no study has used ToF-SIMS or similar MS imaging techniques to detect indigenous biomarkers in kerogenous sediments. The goal of this study is to use GC-MS analysis to guide the interpretation of ToF-SIMS datasets collected on a Jurassic (Callovian), organic-rich, thermally immature sediment sample in order to determine the capabilities of ToF-SIMS for analysis of indigenous lipid biomarkers in a kerogen-rich sedimentary matrix.

2. Materials and Methods

2.1 Samples

The sample analyzed here, P89-13 (Fig. 2), was sampled in the Dogsthorpe brick pit from the Peterborough Member of the Oxford Clay Formation, a Jurassic (~164 million-year-old), organic carbon- and sulfur-rich marine argillaceous sediments that contains very thermally immature Type-II kerogen (Kenig *et al.,* 1994). This sample contains 14.2 wt. % total organic carbon (TOC), 4.2 wt.% sulfur, and 1.2 wt.% carbonate (Kenig *et al.,* 1994;). Organic geochemical analysis presented here were obtained on sample P90-1, which was sampled just below sample P89-13 in the same bed (Bed 10) at the Dogsthorpe brick pit (Kenig *et al.,* 1994). P90-1 contains 12.1 wt. % of TOC, 3.5 wt. % sulfur, and 1.7 wt. % carbonate and, like for sample P89-13, its biofacies was described as deposit feeder bituminous shale by Duff (1975). Because the Oxford Clay has never been exposed to temperatures above 50°C (Kenig et al. 1994;

Green *et al.,* 2001), molecular biomarkers within the sediments have not migrated through the sediments and should therefore be found in place.

2.2 GC-MS analysis.

Powdered rock samples were Soxhlet extracted with DCM/MeOH (7.5:1) for 72 hours. The extracted bitumen was then fractionated according to procedures described in Simons and Kenig (2001). Here we present GC-MS results from the saturated/unsaturated hydrocarbon fraction (SUHF) and aromatic hydrocarbon fraction (AHF) of the apolar bitumen. GC-MS analysis was performed on a Hewlett Packard 6890 gas chromatograph (GC) coupled to a HP-5973 mass-selective detector operated in electron ionization (EI) mode at 70 eV. The GC injector was operated in splitless mode and was connected to an HP-5MS fused-silica capillary column (30 m × 0.25 mm, film thickness 0.25 μm). The oven temperature was programmed from 60°C, held for 1.5 minutes, then to 130°C at 20°C/ minute, and finally to 315°C at 4°C/ minute, which was then held for 60 minutes. Tentative identification of the components is based on the comparison of their mass spectra and relative retention time with those published in the literature (Esminger *et al.,* 1978; Brassell *et al.,* 1984; Peakman and Maxwell, 1988; Peters and Moldowan,1993; Kenig *et al.,* 1995; Koopmans *et al.,* 1996; Koopmans *et al.,* 1997; van Kaam Peters *et al.,* 1997; Köster *et al.,* 1998; Sinninghe Damsté *et al.,* 2014).

2.3 Sample Preparation for MSI Analysis.

Samples were prepared using techniques described in detail in Wickramasinghe et al. (2021). Briefly, a rock chip was cut and polished on one side, attached to a pre-cleaned (washed with detergent and deionized water, then triple rinsed with DCM/MeOH, 1:1) indium tin oxide glass slide using conductive Ag epoxy. The sample was then re-cut, ground and polished to obtain a final uncovered rock section with a thickness of ~70 μm. The sample was prepared to expose regions perpendicular to the sedimentary bedding planes.

A low-speed saw (Isomet II-1180, Buehler, IL, USA) with a washed and DCM/ MeOH (1:1) triple-rinsed diamond-tipped wafering blade (IsoMet Blade, 20LC, Buehler, IL, USA) was

used for all cutting. The saw was retrofitted with removable, bakeable parts to eliminate cutting water interaction with paint; all parts were washed with laboratory detergent, triple-rinsed in deionized water, and baked for 12 hours at 500ºC prior to use. Custom made cast ion lapping wheels and glass polishing plates were cleaned the same way as the retrofitted saw parts. Silicon carbide powder grit 320 and 120 (CarbiMet Plain, Buehler, IL, USA; baked at 500°C for 12 hours) were used for lapping and deagglomerated alpha alumina (MicroPolish II Suspension, Buehler, IL, USA; baked at 500°C for 12 hours) 1 and 0.3 μm were used for polishing the rock section. Chromic acid distilled water was the only lubricant for cutting, grinding, and polishing. To track possible migration paths for contaminants, 1 mg/100 mL of analytical grade sulfanilamide (>98.0% purity, Sigma-Aldrich Inc. St. Louis, MO) was added to this distilled water. Portions of the cutting/grinding water were collected and extracted three times with *n*-hexanes (1:3 v/v), concentrated to 3-5 mL using a rotary evaporator, then fully evaporated under nitrogen and re-dissolved in cyclohexane (99.99% purity, Fisher Chemical, Waltham, MA) at a concentration of 1 mg sample/100μL cyclohexane, and analyzed via GC-MS to monitor for possible contamination.

The mounted mudstone section was cleaned using a narrow nozzle CO_2 snow-jet cleaner (High Purity Unit K4-10, Applied Surface Technologies, New Providence, NJ). Instrument grade CO_2 gas (Anaerobic grade 4.0, Praxair, Danbury, CT) filtered through an H_2O and hydrocarbon trap (P600-2, Vici high pressure CO_2 gas purifier, VICI Metronics, Poulsbo, WA) was used for cleaning. The section was placed in a washed and baked (500°C for 12 hours) petri dish, wrapped in baked aluminum foil (500°C for 12 hours), and placed in a covered container for storage. The section was cleaned again using the CO_2 snow-cleaning system prior to ToF-SIMS analysis at Oak Ridge National Laboratory.

2.4 Optical Imaging, SIMS Imaging and Data Analysis.

High-resolution optical micrographs were collected before MS imaging analysis. Optical micrographs of the whole sample surface (before MS imaging) and the target regions (before and after MS imaging) were collected using a high-resolution stereoscope (Leica M 205 C) coupled to a color microscope camera (Leica DFC495, operated via Leica Application Suite software package).

ToF-SIMS experiments were performed on an IONTOF TOF.SIMS 5 NCS instrument (IONTOF GmbH, Münster, Germany), equipped with a 30 keV maximum energy bismuth cluster liquid metal ion source (LMIS) and a 20 keV maximum energy argon gas cluster ion source (GCIS). The ToF-SIMS was operated in spectrometry mode, with 100 µs cycle time for the ToF mass analyzer (max. *m/z* 0 - 900). Manually defined sampling locations were sputter-cleaned using an Ar_{2200} gas cluster ion beam (6.7 nA beam current) to expose areas of 800 µm × 800 µm (2 frames, 2.9 s total sputter time) prior to data acquisition. An analysis beam of Bi_3^+ primary ions (29.2 nA DC current) was used to image areas of 500 µm × 500 µm. Spectra of 256 × 256 imaging pixels were acquired in a random scan pattern for each frame (6.6 s total acquisition time per frame), with 150 frames recorded for each analyzed region. Negative and positive polarity spectra were recorded at each sampling location. MS imaging data were exported to GRD file format using IONTOF SurfaceLab 7 and converted into imzML format using the open-source software imzMLConverter (University of Birmingham, Edgbaston, Birmingham, UK; Race *et al.,* 2012). Converted data were analyzed using the open-source software Datacube Explorer (AMOLF, Amsterdam, Netherlands; Klinkert *et al.,* 2013).

2.5 Accounting for surface topography and the standard deviation of ions.

During ToF-SIMS, an irregular surface can lead to a reduction in mass accuracy and mass resolution (Lee *et al.,* 2011a; Lee *et al.,* 2011b). The vertical scale of surface topography for our polished sample was determined by measuring the difference between optimal focus of the upper and lower portions of the targeted regions using the digital readout of the objective lens height using a digital Leica M 205 C binocular microscope (described above). The Oxford clay thick section had an average surface topography spanning 10.9 µm (n = 40; σ = 6.4) within the analyzed boxes. Difference in height below 15 µm is sufficient to maintain both good mass resolution and mass accuracy (Lee *et al.,* 2011a), so deviation of masses will be minimal for our sample. We calculated the ion standard deviation (SD) for this sample by collecting spectra containing silver ions Ag_2^+, Ag_3^+, and Ag_5^+ (*m/z* 213.8/ 215.8/ 217.8, *m/z* 320.7/ 322.7/ 324.7/ 326.7, and *m/z* 534.5/ 536.5/ 538.5/ 540.5/ 542.5 respectively) from 14 locations across the sample. The average standard deviation of ions analyzed here was SD = 0.06 with an increase in

variance with increasing mass from Ag_2^+ (average SD = 0.05, maximum SD = 0.09) to Ag_5^+ (average SD = 0.08, maximum SD = 0.14), consistent with topography-driven effects (Lee *et al.,* 2011a). The observed topography driven SD means that all ions observed within our spectra can be expected to have an average deviation of *m/z* 0.06 from the true mass with an expected maximum deviation of *m/z* 0.14. Difference in topography also affects the relative abundance of analytes with different masses (Lee et al. 2011a). As a result, scanning electron microscope (SEM) images of the analyzed surface were collected to confirm the absence of large variations in topography in the analyzed regions.

2.6 Scanning electron microscopy.

SEM images displaying topography were acquired using secondary electron detection in backscatter electron detection - topography (BED-T) mode. The field emission scanning electron microscope JSM-IT500HR InTouchScope™ (JEOL Ltd., Tokyo, Japan) was used with a 15 kV acceleration voltage, a probe current of 50 (arbitrary scale), and a working distance of 10.6 mm. Images were acquired under high vacuum (1×10^{-5} bar) conditions at normal or 65º off-normal incidence with magnification of ×170.

3. Results

3.1 Gas Chromatography-Mass Spectrometry.

The SUHF of sample P90-1 is dominated by chlorophyl-derived pristane and phytane (Kenig *et al.,* 1994) and short-chain *n*-alkanes (C_{13}-C_{20}) with a mode at *n*-C_{18}. A comparatively minor contribution of long-chain *n*-alkanes (C_{23}-C_{37}) with an odd over even carbon number predominance is detectable (Fig. 3). This fraction also contains algae-derived C_{27} – C_{30} steroid hydrocarbons and early diagenetic derivatives, diasteroids, including steranes, sterenes, 4-methylsteranes, 4-methylsterenes, abundant diasterenes, spirosterenes, 4-methyl diasterenes and 4-methyl spirosterenes (Table 1). Steroid hydrocarbon molecular ions and structures as determined by mass spectral data, retention time and by comparison with published mass spectra (Ensminger *et al.,* 1978; Brassell *et al.,* 1984; Peakman and Maxwell, 1988; Peters and Moldowan,1993; Kenig *et al.,* 1995) are shown in Figure 3. Bacteria derived C_{29}-C_{35} hopanoid

hydrocarbons, hopanes and hopenes, are present but in much lower abundance relative to steroids (Fig. 3). The most abundant hopanoids are the unsaturated hopenes C_{28} 22,30-bisnorhop-13(18)-ene (382 Da, H_1 in Fig. 3; Sinninghe Damsté *et al.,* 2014) and C_{30} Hop-17(21)-ene (410 Da, H_2 in Fig. 3; Köster *et al.,* 1998).

The AHF of sample P90-1 contains methylated naphthalenes and methylated biphenyls but is dominated by isorenieratene derivatives, including isorenieratane (Fig. 4). Isorenieratene is a diaryl carotenoid pigment (ϕ,ϕ-carotene) derived from the brown strain of green sulfur bacteria (Chlorobi). The description of these compounds in the Oxford Clay samples was previously done by Koopmans et al. (1996) and Kenig et al. (2004). Diagenetic derrivatives of isorenieratene were identified by comparing their mass spectra and relative retention time to the data in Koopmans et al. (1996) and van Kaam-Peters et al. (1997). The structure and molecular ions of the dominant isorenieratene derivatives of the AHF of sample P90-1 are shown in Figure 4.

3.2 Mass spectrometry imaging.

MS images were visually compared to the optical micrographs and manually searched to co-register regions of interest including laminated regions, regions containing large grains, and regions containing the silver epoxy used to attach the thick sections to the ITO glass slides. ToF-SIMS MS images and spectra were then interrogated to determine: i) ions that can be used to create MS maps correspding to sample features and regions (Fig. 5A), and ii) potential identities of ions observed from manually defined areas of sample regions.

Silver is the dominant component of spectra collected from epoxy regions (Fig. 5B) with prominent peaks for Ag^+ at *m/z* 106.9 and the isotopic peak of silver at *m/z* 108.9. The strong intensity of the silver ions within epoxy regions allowed us to map those regions using ion *m/z* 106.9 (Ag^+, Fig. 5A). The isotopic doublet of silver produces distinct ions throughout the scanned mass range including Ag_2^+, Ag_3^+, and Ag_5^+ (Fig. 5B, Table 2). Ag_x^+ ions were also observed with varying amounts of O and H (Table 2). We used spectra extracted from the epoxy regions as a direct comparison to all other spectra as a control against any potential contribution of epoxy. The unlaminated yellow grain in Fig. 2 and Fig. 5A is mappable using ion *m/z* 158.9, consistent with $Ca_2PO_3^+$ (Henss *et al.,* 2013; Kleine-Boymann *et al.,* 2014). ToF-SIMS spectra

from the grain display ions consistent with calcium phosphate (Henss *et al.,* 2013; Kleine-Boymann *et al.,* 2014). The phosphate grain is potentially a bone fragment.

We interrogated the ToF-SIMS spectra for fragment and molecular ions consistent with the those observed in GC-MS spectra of the SUHF and AHF. In the ToF-SIMS spectra, many low mass ions, including *m/z* 55.1 and *m/z* 57.1, are present but can be produced by multiple organic and potentially inorganic sources. For example, epoxy used to affix the sample to the conductive slide produces both fragment ions *m/z* 55.1 and *m/z* 57.1 (Fig. 5B), so these ions cannot be used as representative fragment ions of indigenous hydrocarbons. For this reason, we were not able to unambiguously assign identities to fragment ions characteristic of many compounds detectable via GC-MS within the ToF-SIMS spectra including the *n*-alkanes, pristane or phytane from the SUHF (Fig. 3), or the methyl-naphthalenes, methyl-biphenyls, or the molecular ions for low molecular weight isorenieratene derivatives from AHF (Fig. 4). Many of the ions with multiple plausible organic sources are spatially restricted to certain regions of the sample.

Regions mappable with fragment ion *m/z* 119.1 (typical of trimethylbenzene) were distinct from the epoxy regions and the calcium phosphate grain (Fig. 5A). The high intensity of fragment ion *m/z* 119.1 is only present within laminated regions of the sample flanking the calcium phosphate grain in Boxes 1 and 2 (Fig. 5A). The spatial distribution of fragment ion *m/z* 119.1 matches the spatial distributions of other aromatic fragment ions including *m/z* 91.1, *m/z* 105.1 and *m/z* 133.1. Regions defined by the presence of fragment ion *m/z* 119.1 contain prominent signals for ions *m/z* 370.3, *m/z* 372.3, and *m/z* 386.3 with a less prominent but detectable signals for ion *m/z* 384.3, *m/z* 398.3 and *m/z* 400.3 (Fig. 5C). Accounting for the ion mass standard deviation (average 0.06 Da; maximum value 0.14 Da; n =14), ions *m/z* 370.3, *m/z* 372.3, *m/z* 384.3, *m/z* 386.3, *m/z* 398.3 and *m/z* 400.3 match the molecular ions of the C_{27}, C_{28} and C_{29} steroid hydrocarbons observed in the extract of sample P90-1 (Fig. 5C, Fig. 6).

Because the areas defined by relative abundance of the fragment ion *m/z* 119.1 contain potential molecular ions of steroid hydrocarbons, we interrogated the ToF-SIMS spectra extracted from those regions for the diagnostic fragment ions for each class of sterane and

sterene described in Table 1. We were able to observe fragment ions *m/z* 215.1 (sterenes and diasterenes), *m/z* 217.1 (steranes) and *m/z* 231.1 (4-methyl steranes and dinosterane) clearly above the background signal, with *m/z* 215.1 producing a stronger signal than *m/z* 217.1 and *m/z* 231.1 (Fig. 7). Epoxy also produces ions in the in this region of the spectra including ions *m/z* 214.8 and *m/z* 216.8 (Table 2, Fig. 7). Accounting for ion standard deviation (average value = 0.06 Da, maximum value = 0.14 Da), potential steroid daughter ions are distinct from the epoxy ions. Fragment ions *m/z* 257.1 (diasterenes) and *m/z* 271.1 (4-methyl diasterenes), as well as *m/z* 206.1, *m/z* 220.1 and *m/z* 234.1 (C_{27}, C_{28} and C_{29} spirosterenes, respectively) were also observed in the ToF-SIMS spectra, but their abundance was low relative to the background signal (Fig. 7).

The abundance of the individual potential steroid molecular ions is too low to produce meaningful MS images for comparing their spatial distribution. We were able to compare the intensity of the potential C_{27}, C_{28}, and C_{29} steroids in 12 different locations across the sample surface by extracting and comparing point spectra (~50 pixels, total image area is 65,536 pixels) from regions which display spectra with abundant fragment ion *m/z* 119.1 (Fig. 8). Ions *m/z* 370.3, *m/z* 372.2, *m/z* 384.3, and *m/z* 386.3 vary independently from point-to-point, with *m/z* 386.3 generally being the most abundant peak in 8 of the 12 spectra presented in Fig. 8.

In the ToF-SIMS spectra we analyzed, we have not been able to observe molecular ions consistent with those of hopanoid hydrocarbons observed by GC-MS in the extract. It is important to note that neither trisnorhopanes, *m/z* 370.3, bisnorhopane, nor methylhopane (*m/z* 384.3 if saturated) were observed in the extract of P90-1. However, in the ToF-SIMS spectra, we observed fragment ions *m/z* 191.1 and *m/z* 205.1 that may be attributable to hopenes, hopanes, and homohopanes as well as methylhopanes (Fig. 7).

Potential fragment ions for isorenieratene derivatives were observed in the ToF-SIMS spectra from areas mappable with fragment ion *m/z* 119.1 including *m/z* 133.1, *m/z* 171.1 and *m/z* 237.1 (Fig. 9B). Cesium (molecular weight 132.91 Da.) was previously used as an ion source in the ToF-SIMS instrument utilized for this analysis leading to Cs deposition within the vacuum chamber, and eventually artefactual deposition onto the sample surface during analysis. Cs produces a strong signal at *m/z* 132.9 in all analyzed regions. Fragment ion *m/z* 133.1 is present

as a shoulder on the Cs peak in the average ToF-SIMS spectra of areas defined by the presence of fragment ion *m/z* 119.1 (Fig. 9B), but no such shoulder is observed in any other region of the sample. Similarly, fragment ions *m/z* 171.1 and *m/z* 237.1 are also above background in the spectra obtained from regions defined by the presence of the fragment ion *m/z* 119.1 (Fig. 9B). A small signal of the molecular ion of isorenieratane (*m/z* 546.4) is present in the same regions (Fig. 9B). The abundance of *m/z* 546.4 relative to *m/z* 133.1 in the ToF-SIMS spectra is similar to that observed in the summed GC-MS spectra (5 to 70 min; Fig. 9B). All fragment ions of isorenieratene derivatives are accompanied by a fragment ion of +2 Da (Fig. 9B). For example, *m/z* 133.1 is paired with a more intense fragment ion *m/z* 135.1 (Fig. 9 A and B). MS maps of the *m/z* 135.1 are more readily co-registered with host-rock features observed in the micrographs than MS maps either of *m/z* 119.1 or *m/z* 133.1 (Fig. 9A). The +2 Da fragment ions are also present for fragment ions of other aromatic compounds such as *m/z* 105 and *m/z* 119.1, di- and tri-methylated benzene, respectively.

4. Discussion

Samples P89-13 and P90-1 are vertically contiguous, have identical biofacies, very similar organic matter and total sulfur contents, hydrogen index values, oxygen index values, carbon isotopic values, total carbon wt. %, and carbonate wt. %. (Kenig et al. 1994); therefore, it seems unlikely that the biomarker distribution in these two samples varies significantly making P90-1 a good proxy for P89-13. GC-MS data obtained on the saturated hydrocarbon fraction of P89-13 (Kenig, unpublished results) also shows the similarity between samples P89-13 and P90-1. One major consideration is whether the content of the SUHF and AHF fractions is reflective of what is ionized and detected upon ToF-SIMS analysis.

It is well known that the SUHF only shows a minor portion of the steroids present in samples containing a polysulfide bound macromolecule (Kohnen *et al.,* 1991; Kenig *et al.,* 1995). Koopmans et al. (1996) has demonstrated that the samples from the Peterborough Member of the Oxford clay contain a polysulfide bound macromolecule that releases abundant isorenieratene derivatives upon Raney Nickel desulfurization and subsequent hydrogenation of the polar fraction. Samples from the Peterborough Member of the Oxford clay also include abundant isorenieratene derivatives in the free aromatic fraction (Kenig *et al.,* 2004). Kohnen et

al. (1991) had already demonstrated that desulfurized maltenes (total extract without the asphaltene fraction) provide orders of magnitude more phytane, steroids and isorenieratene derivatives than observed in the free hydrocarbon fraction (here the SUHF and AHF). The major difference between the distribution of steroids in the S-bound macromolecule and in the free fraction, is that the free fraction includes early diagenetic derivatives including clay catalyzed diasterenes, 4-methyldiasterenes, and spirosterenes that are all absent in the S-bound macromolecule; such diagenetic processes do not affect the steroids of the bound fractions (Bowden *et al.,* 2006). During ToF-SIMS, the material ionized may derive from both the free and the bound fractions, as well as from the kerogen, thus we cannot expect a similar distribution of steroids in the SUHF analyzed by GC-MS (free steroids) and the steroids that are ionized during ToF-SIMS.

In previous ToF-SIMS analyses of steroid hydrocarbons, individual sterane standards drop-cast on Si wafers primarily ionized via the loss of an H atom forming an $[M\text{-}H]^+$ ion, but exhibited fragmentation patterns similar to those observed in 70 eV EI (Sjövall *et al.,* 2008; Leefmann *et al.,* 2013). The $[M\text{-}H]^+$ ion and diagnostic daughter ions *m/z* 217 and *m/z* 257 were also observed via ToF-SIMS in both crude oils and within fluid inclusions (Siljeström *et al.,* 2009; 2010; 2013). In our ToF-SIMS spectra, M^+ was the dominant ion observed for each of the potential steroids with no detectable $M\text{-}H^+$, $M+H^+$, or $M\text{-}CH_3^+$ (Fig. 6) as would be expected from previous ToF-SIMS analysis of steranes (Sjövall *et al.,* 2008; Siljeström *et al.,* 2009; Siljeström *et al.,* 2010; Leefmann *et al.,* 2013; Siljeström *et al.,* 2013). Steele et al. (2001) found that while the $[M\text{-}H]^+$ ion was the dominant ion produced by individual hopanoid biomarkers analyzed via ToF-SIMS, $[M]^+$ ions were dominant for those same biomarkers in lipid mixtures; and it can be speculated that a similar effect may be responsible for the dominance of the $[M]^+$ ions here.

Because we monitored for contamination throughout sample preparation, we are confident that no steroid biomarkers were incorporated into or onto the sample prior to or during sample preparation. If the ions observed here are contaminants, they would have been introduced onto the sample surface via laboratory air immediately prior to analysis after CO_2 snow-jet cleaning. If this were the case, the ions should be randomly distributed across the sample surface

rather than being restricted to specific host-rock features. Instead, these ions were only detectable in select regions (Fig. 5) flanking the calcium phosphate grain.

The occurrence of molecular ions *m/z* 370.3, *m/z* 372.3, *m/z* 384.3, and *m/z* 386.3 in ToF-SIMS spectra is consistent with saturated and unsaturated steroid hydrocarbons observed in the SUHF (Fig. 3 and Fig. 6), supporting their assignment as indigenous steroid hydrocarbons. The dominant diagnostic sterane daughter ions observed in GC-MS spectra of the SUHF fraction of sample P90-1 are *m/z* 257 (diasterene), *m/z* 271 (methyl-diasterene), *m/z* 217 (saturated steranes) and *m/z* 231 (methyl-steranes), with *m/z* 257 and *m/z* 271 being more abundant than *m/z* 217 and *m/z* 231 (Fig. 3). In the ToF-SIMS spectra containing potential steroid molecular ions, we observe daughter ions *m/z* 215, *m/z* 217 and *m/z* 231 above background levels (Fig. 7). The absence of clay catalyzed diagenetic diasterenes, methyl-diasterenes and spirosterenes in the bound fractions (S-Bound, kerogen bound) plausibly explains why daughter ions of diasteroids and spirosteroids are less prominent in the ToF-SIMS spectra. Daughter ions diagnostic of steroids and ions *m/z* 370.3, *m/z* 372.3, *m/z* 384.3, and *m/z* 386.3 observed in the same ToF-SIMS spectra further supports their assignment as molecular ions of steroid hydrocarbons. Still, C_{27} cholestane (*m/z* 372.3) is the only steroid that has only 1 potential peak assignment (Table 1) and can therefore be assigned an identity with some degree of certainty. The strong signal observed at ion *m/z* 386.3 may be a mixture of C_{28} 4-methyl-cholestane and C_{28} 24-methyl-cholestane as indicated in Table 1.

There are large differences in the relative abundance of the molecular ions of these potential steroids in different areas of the MS images of Boxes 1 and 2 (Fig. 7). These differences could be the result of changes in surface topography, which results in ions being deflected from the sample at high angles relative to the detector (Lee *et al.,* 2011a). This high-angle deflection leads to a decreased relative abundance of higher masses relative to lower masses due to difference in kinetic energy (Lee *et al.,* 2011a). Point spectra (~50 pixels) labelled 1, 2, and 3 (Fig. 8) were all extracted from regions of the sample with sub-micron topography that would not affect the relative abundance of ions produced from those points (Fig. 8C). The relative abundance of *m/z* 372.3 is higher than *m/z* 386.3 in spectrum 1, while this pattern is reversed in spectra 2 and 3. This indicates that the differences in abundance of the ions within

each targeted region is driven by fine-scale heterogeneity of the abundance of steroids rather than by surface topography alone. Sample heterogeneity at the scale of 10's to 100's of microns is at least one factor controlling the relative abundance of potential steroids.

The observation of fragment ions *m/z* 133.1, *m/z* 171.1 and *m/z* 237.1 and the presence of the molecular ion of isorenieratene in ToF-SIMS spectra collected from areas with a signal for *m/z* 119.1 (Fig. 9) is consistent with the presence of these ions in the GC-MS spectra of the AHF where abundant isorenieratene derivatives were identified (Fig. 3). The fragment ions of isorenieratene derivatives and methylbenzenes (dimethylbenzene, trimethylbenzene) were all associated with +2 Da fragment ions. Toporski and Steele (2004) observed such a $[M+2]^+$ ion produced upon ToF-SIMS of pyrene both when isolated and when mixed with other compounds. This suggests that aromatic fragment ions and molecular ions can be recognized in ToF-SIMS using this characteristic rearrangement.

No molecular ion was detectable for any hopanoids in the ToF-SIMS spectra. We were able to detect potential hopanoid fragments ions *m/z* 191.1 and *m/z* 205.1 (Fig. 7), but the lack of a molecular ion also limits these assignments to very tentative. Unlike the isorenieratene derivatives, hopanoids only compose a minor amount of the extractable fraction observed via GC-MS, so that their molecular ions are not observed here is not surprising.

MS-imaging of lipid biomarkers show the strong heterogeneity of their distribution within an ancient sediment sample (Fig. 8). The biomarkers are generally found in organic matter-rich lamina but not all organic matter-rich lamina contain the same distribution of biomarkers. The heterogeneity extends to the distribution of biomarkers within organic matter-rich laminae themselves (Fig. 8). Here, we have studied a very organic matter-rich mudstone (14.2 wt. % TOC). Some areas of the sample are completely devoid of biomarkers, and in contrast, some small areas seem to concentrate them. These observations suggests that biomarkers may be detected via MS-imaging in even low TOC sediments if the biomarkers are present in concentrated areas. This result has implications for the Earth-based MS imaging analysis of geological material, including the analysis of samples returned from Mars.

Conclusions.

GC-MS data from the solvent extract of the organic carbon-rich Peterborough member of the Oxford clay is useful to guide the interpretation of MS imaging datasets obtained via ToF-SIMS of a carefully prepared geologic thick-section. The organic extract analyzed via GC-MS contains abundant and diverse C_{27} – C_{30} steroid hydrocarbons, abundant isorenieratene derivatives and a minor contribution of hopanoid hydrocarbons. Within ToF-SIMS datasets, potential C_{27}, C_{28} and C_{29} steroid molecular ions and steroid daughter ions were observed. All potential ions derived from steroids are restricted to laminated regions flanking a phosphate grain, indicating that the ions are indigenous steroid hydrocarbons. The steroid hydrocarbon distribution we observed in the ToF-SIMS spectra is similar to the steroid hydrocarbons we observed via GC-MS, but they are not a direct correlation. While all steroids we observed in the ToF-SIMS datasets were observed in the GC-MS datasets, the relative abundance of the steroids detectable in both datasets was not the same. Heterogeniety of individual steroids at the scale of 10's to 100's of microns is one factor that affects the relative abundance of indigenous steroids in ToF-SIMS spectra. Fragment ions of isorenieratene derivatives including *m/z* 133.1, *m/z* 171.1, and *m/z* 237.1, and a small molecular ion of isorenieratane at *m/z* 546.4 are also present in ToF-SIMS spectra extracted from same regions as the steroid hydrocarbons. All isorenieratene fragment ions as well as methylbenzene ions were accompanied by a +2 Da peak. The +2 Da peak could be useful for identifying and mapping aromatic fragment ions in future analyses. We observed potential hopanoid hydrocarbon fragment ions but no potential molecular ions. The results presented here indicate that the concentration of organic matter in a given location may be more important for biomarker detection via ToF-SIMS and MS imaging than the total organic carbon content of a rock or sediment. Future analyses should target low TOC rocks and sediments with areas of concentrated organic matter to constrain the abilitiy of ToF-SIMS to detect biomarkers, including in samples returned from Mars.

Funding Information:

This research was supported by grant NASA NNX17AK88G to FK and LH.

Acknowledgements:

We all thank the UIC Research Resources Center for access to the Electron Microcopy Core.

Author Contributions:

M.J.P. conceptualize project development, produced figures and text, prepared samples for ToF-SIMS analysis, helped in ToF-SIMS data collection, and conducted data analysis for all datasets. R.C.W. helped with ToF-SIMS data collection and analysis and data interpretation. A.V.I. and M.L. were the primary operators of the ToF-SIMS instrument at the Center for Nanophase Materials Science within the Oak Ridge National Laboratories. LH. conceptualized project development, ToF-SIMS analysis, and oversaw data interpretation. F.K. conceptualized project development, oversaw GC-MS analysis, the interpretation of GC-MS spectra, sample preparation, data interpretation, manuscript preparation and figure preparation.

Conflicts of Interest:

The authors declare no competing financial interest.

Data Access:

The large volume of data produced as part of the work presented within this manuscript is unfortunately too large to be stored in a free, public repository. Additionally, there is currently no free database for hosting MS images. All data presented within this thesis will be available to any parties upon request. When a free database becomes available to store the data presented here, the data will be archived for free use.

References.

Beaty DW, Grady MM, McSween HY, et al. The Potential Science and Engineering Value of Samples Delivered to Earth by Mars Sample Return: International MSR Objectives and Samples Team (IMOST). Meteorit Planet Sci 2019;54(S1):S3–S152; doi: 10.1111/maps.13242.

Bowden SA, Farrimond P, Snape CE, et al. Compositional Differences in Biomarker Constituents of the Hydrocarbon, Resin, Asphaltene and Kerogen Fractions: An Example from the Jet Rock (Yorkshire, UK). Org Geochem 2006;37:369–383; doi: 10.1016/j.orggeochem.2005.08.024.

Brassell SC, McEvoy J, Hoffmann CF, et al. Isomerisation, Rearrangement and Aromatisation of Steroids in Distinguishing Early Stages of Diagenesis. Org Geochem 1984;6:11–23; doi: 10.1016/0146-6380(84)90022-6.

Brocks JJ. Millimeter-Scale Concentration Gradients of Hydrocarbons in Archean Shales: Live-Oil Escape or Fingerprint of Contamination? Geochim Cosmochim Acta 2011;75(11):3196–3213; doi: 10.1016/j.gca.2011.03.014.

Cloutis EA. Styles of Aqueous Alteration on Mars. Am Mineral 2016;101(August):1925–1926; doi: 10.1029/2007GL031267.Cloutis.

Duff, K. L. Palaeoecology of a bituminous shale - the Lower Oxford Clay of Central England. Palaeontology 1975;18:443-482.

Ehlmann BL, Mustard JF, Fassett CI, et al. Clay Minerals in Delta Deposits and Organic Preservation Potential on Mars. Nat Geosci 2008;1(6):355–358; doi: 10.1038/ngeo207.

Ensminger, A., Joly, G., and Albrecht, P. Rearranged Steranes in Sediments and Crude Oils. Tetrahedron Letters 1978;8:1575 - 1578.

Farley KA, Williford KH, Stack KM, et al. Mars 2020 Mission Overview. Space Sci Rev 2020;216(8); doi: 10.1007/s11214-020-00762-y.

Gilmore IS. SIMS of Organics—Advances in 2D and 3D Imaging and Future Outlook. J Vac Sci Technol A Vacuum, Surfaces, Film 2013;31(5):050819; doi: 10.1116/1.4816935.

Goudge TA, Mohrig D, Cardenas BT, et al. Stratigraphy and Paleohydrology of Delta Channel Deposits, Jezero Crater, Mars. Icarus 2018;301:58–75; doi: 10.1016/j.icarus.2017.09.034.

Green PF, Thomson K and Hudson JD. Recognition of Tectonic Events in Undeformed Regions: Contrasting Results from the Midland Platform and East Midlands Shelf, Central England. J Geol Soc London 2001;158(1):59–73; doi: 10.1144/jgs.158.1.59.

Hanley L, Wickramasinghe R and Yung YP. Laser Desorption Combined with Laser Postionization for Mass Spectrometry. Annu Rev Anal Chem 2019;12:225–245; doi: 10.1146/annurev-anchem-061318-115447.

Heim C, Sjövall P, Lausmaa J, et al. Spectral Characterisation of Eight Glycerolipids and Their Detection in Natural Samples Using Time-of-Flight Secondary Ion Mass Spectrometry. Rapid Commun Mass Spectrom 2009;23:2741–2753; doi: 10.1002/rcm.

Henss A, Rohnke M, Khassawna T El, et al. Applicability of ToF-SIMS for Monitoring Compositional Changes in Bone in a Long-Term Animal Model. J R Soc Interface 2013;10(86); doi: 10.1098/rsif.2013.0332.

Ivarsson, M., Broman, C., Sturkell, E., Ormo, J., Siljeström, S., and Bengtson, S. Fungal colonization of an Ordovician impact-induced hydrothermal system. Scientific Reports 2013;3:1–6.

Kenig F, Hayes JM, Popp BN, et al. Isotopic Biogeochemistry of the Oxford Clay Formation (Jurassic), UK. J Geol Soc London 1994;151:139–152.

Kenig F, Hudson JD, Damsté JSS, et al. Intermittent Euxinia: Reconciliation of a Jurassic Black Shale with Its Biofacies. Geology 2004;32(5):421–424; doi: 10.1130/G20356.1.

Kenig F, Sinninghe Damsté JS, Frewin NL, et al. Molecular Indicators for Palaeoenvironmental Change in a Messinian Evaporitic Sequence (Vena Del Gesso, Italy): II. High-Resolution Variations in Abundances and 13C Contents of Free and Sulphur-Bound Carbon Skeletons in a Single Marl Bed. Org Geochem 1995;23(6):485–526; doi: 10.1016/0146-6380(95)00041-C.

Kleine-Boymann M, Rohnke M, Henss A, et al. Discrimination between Biologically Relevant Calcium Phosphate Phases by Surface-Analytical Techniques. Appl Surf Sci 2014;309:27–32; doi: 10.1016/j.apsusc.2014.04.129.

Klinkert I, Chughtai K, Ellis SR, et al. Methods for Full Resolution Data Exploration and Visualization for Large 2D and 3D Mass Spectrometry Imaging Datasets. Int J Mass Spectrom 2014;362:40–47; doi: 10.1016/j.ijms.2013.12.012.

Kohnen MEL, Sinninghe Damste JS and De Leeuw JW. Biases from Natural Sulphurization in Palaeoenvironmental Recon- Struction Based on Hydrocarbon Biomarker Distributions. Nature 1991;349(February):775–778.

Koopmans MP, Köster J, Van Kaam-Peters HME, et al. Diagenetic and Catagenetic Products of Isorenieratene: Molecular Indicators for Photic Zone Anoxia. Geochim Cosmochim Acta 1996;60(22):4467–4496; doi: 10.1016/S0016-7037(96)00238-4.

Koopmans MP, De Leeuw JW and Sinninghe Damsté JS. Novel Cyclised and Aromatised Diagenetic Products of β-Carotene in the Green River Shale. Org Geochem 1997;26(7–8):451–466; doi: 10.1016/S0146-6380(97)00025-9.

Köster J, Rospondek M, Schouten S, et al. Biomarker Geochemistry of a Foreland Basin: The Oligocene Menilite Formation in the Flysch Carpathians of Southeast Poland. Org Geochem 1998;29(1-3–3):649–669; doi: 10.1016/S0146-6380(98)00182-X.

Lauzon N, Dufresne M, Chauhan V, et al. Development of Laser Desorption Imaging Mass Spectrometry Methods to Investigate the Molecular Composition of Latent Fingermarks. J Am Soc Mass Spectrom 2015;26(6):878–886; doi: 10.1007/s13361-015-1123-0.

Lee H, Shokouhimehr M, Ostadhassan M, et al. Molecular Weight Distribution of Kerogen with MALDI-TOF-MS. ChemRxiv 2019;(1); doi: 10.26434/chemrxiv.10565441.v1.

Lee JLS, Gilmore IS, Seah MP, et al. Topography and Field Effects in Secondary Ion Mass Spectrometry - Part I: Conducting Samples. J Am Soc Mass Spectrom 2011;22(10):1718–1728; doi: 10.1007/s13361-011-0201-1.

Lee JLS, Gilmore IS, Seah MP, et al. Topography and Field Effects in Secondary Ion Mass Spectrometry Part II: Insulating Samples. Surf Interface Anal 2012;44(2):238–245; doi: 10.1002/sia.3833.

Leefmann T, Heim C, Kryvenda A, et al. Biomarker Imaging of Single Diatom Cells in a Microbial Mat Using Time-of-Flight Secondary Ion Mass Spectrometry (ToF-SIMS). Org Geochem 2013a;57:23–33; doi: 10.1016/j.orggeochem.2013.01.005.

Leefmann T, Heim C, Siljeström S, et al. Spectral Characterization of Ten Cyclic Lipids Using Time-of-Flight Secondary Ion Mass Spectrometry. Rapid Commun Mass Spectrom 2013b;27(5):565–581; doi: 10.1002/rcm.6483.

Li C -Z, Herod AA, John P, et al. Characterization of Kerogens by Matrix-assisted Laser Desorption Ionization Mass Spectroscopy. Rapid Commun Mass Spectrom 1994;8(10):823–828; doi: 10.1002/rcm.1290081006.

Li X, Danell RM, Pinnick VT, et al. Mars Organic Molecule Analyzer (MOMA) Laser Desorption/Ionization Source Design and Performance Characterization. Int J Mass Spectrom 2017;422:177–187; doi: 10.1016/j.ijms.2017.03.010.

Massonnet P and Heeren RMA. A Concise Tutorial Review of TOF-SIMS Based Molecular and Cellular Imaging. J Anal At Spectrom 2019;34(11):2217–2228; doi: 10.1039/c9ja00164f.

Medina Ferrer F, Bailey J V., Corsetti F, et al. Assessing Biomarker Syngeneity: An in Situ Approach Using Monoclonal Antibodies. Org Geochem 2018;124:112–122; doi: 10.1016/j.orggeochem.2018.05.006.

Neveu M, Hays LE, Voytek MA, et al. The Ladder of Life Detection. Astrobiology 2018;18(11):1375–1402; doi: 10.1089/ast.2017.1773.

Noun M, Baklouti D, Brunetto R, et al. A Mineralogical Context for the Organic Matter in the Paris Meteorite Determined by a Multi-Technique Analysis. Life 2019;9(2); doi: 10.3390/life9020044.

Paine MRL, Kooijman PC, Fisher GL, et al. Visualizing Molecular Distributions for Biomaterials Applications with Mass Spectrometry Imaging: A Review. J Mater Chem B 2017;5(36):7444–7460; doi: 10.1039/c7tb01100h.

Peakmanm TM and Maxwell JR. Early Diagenetic Pathways of Steroid Alkenes. Org Geochem 1988;13:583–592.

Peters, K.E. and Moldowan, J.M. The Biomarker Guide, Interpreting Molecular Fossils in Petroleum and Ancient Sediments. Prentice Hall, Inc, Englewood Cliffs, NJ; 1993.

Race AM, Styles IB and Bunch J. Inclusive Sharing of Mass Spectrometry Imaging Data Requires a Converter for All. J Proteomics 2012;75(16):5111–5112; doi: 10.1016/j.jprot.2012.05.035.

Siljeström S, Hode T, Lausmaa J, et al. Detection of Organic Biomarkers in Crude Oils Using ToF-SIMS. Org Geochem 2009;40(1):135–143; doi: 10.1016/j.orggeochem.2008.08.010.

Siljeström S, Lausmaa J, SjÖvall P, et al. Analysis of Hopanes and Steranes in Single Oil-Bearing Fluid Inclusions Using Time-of-Flight Secondary Ion Mass Spectrometry (ToF-SIMS). Geobiology 2010;8(1):37–44; doi: 10.1111/j.1472-4669.2009.00223.x.

Siljeström S, Parenteau MN, Jahnke LL, et al. A Comparative ToF-SIMS and GC–MS Analysis of Phototrophic Communities Collected from an Alkaline Silica-Depositing Hot Spring. Org Geochem 2017;109:14–30; doi: 10.1016/j.orggeochem.2017.03.009.

Siljeström S, Volk H, George SC, et al. Analysis of Single Oil-Bearing Fluid Inclusions in Mid-Proterozoic Sandstones (Roper Group, Australia). Geochim Cosmochim Acta 2013;122:448–463; doi: 10.1016/j.gca.2013.08.010.

Simons DJH and Kenig F. Molecular Fossil Constraints on the Water Column Structure of the Cenomanian-Turonian Western Interior Seaway, USA. Palaeogeogr Palaeoclimatol Palaeoecol 2001;169(1–2):129–152; doi: 10.1016/S0031-0182(01)00222-X.

Sinninghe Damsté JS, Schouten S and Volkman JK. C27-C30 Neohop-13(18)-Enes and Their Saturated and Aromatic Derivatives in Sediments: Indicators for Diagenesis and Water Column Stratification. Geochim Cosmochim Acta 2014;133:402–421; doi: 10.1016/j.gca.2014.03.008.

Sjövall P, Bake KD, Pomerantz AE, et al. Analysis of Kerogens and Model Compounds by Time-of-Flight Secondary Ion Mass Spectrometry (TOF-SIMS). Fuel 2021;286(October 2020):1–17; doi: 10.1016/j.fuel.2020.119373.

Sjövall P, Thiel V, Siljeström S, et al. Organic Geochemical Microanalysis by Time-of-Flight Secondary Ion Mass Spectrometry (ToF-SIMS). Geostand Geoanalytical Res 2008;32(3):267–277; doi: 10.1111/j.1751-908X.2008.00909.x.

Steele A, Toporski JKW, Avci R, et al. Time of Flight Secondary Ion Mass Spectrometry (ToFSIMS) of a Number of Hopanoids. Org Geochem 2001;32(7):905–911; doi: 10.1016/S0146-6380(01)00048-1.

Stephan T. TOF-SIMS in Cosmochemistry. Planet Space Sci 2001;49(9):859–906; doi: 10.1016/S0032-0633(01)00037-X.

Stephan T, Jessberger EK, Heiss CH, et al. TOF-SIMS Analysis of Polycyclic Aromatic Hydrocarbons in Allan Hills 84001. Meteorit Planet Sci 2003;38(1):109–116; doi: 10.1111/j.1945-5100.2003.tb01049.x.

Stephan T, Rost D, Vicenzi EP, et al. TOF-SIMS Analysis of Cometary Matter in Stardust Aerogel Tracks. Meteorit Planet Sci 2008;43(1–2):233–246; doi: 10.1111/j.1945-5100.2008.tb00619.x.

Thiel V, Blumenberg M, Kiel S, et al. Occurrence and Fate of Fatty Acyl Biomarkers in an Ancient Whale Bone (Oligocene, El Cien Formation, Mexico). Org Geochem 2014;68:71–81; doi: 10.1016/j.orggeochem.2013.12.006.

Thiel V, Heim C, Arp G, et al. Biomarkers at the Microscopic Range: ToF-SIMS Molecular Imaging of Archaea-Derived Lipids in a Microbial Mat. Geobiology 2007;5(4):413–421; doi: 10.1111/j.1472-4669.2007.00119.x.

Thiel V and Sjövall P. Using Time-of-Flight Secondary Ion Mass Spectrometry to Study Biomarkers. Annu Rev Earth Planet Sci 2011;39:125–156; doi: 10.1146/annurev-earth-040610-133525.

Toporski J and Steele A. Characterization of Purified Biomarker Compounds Using Time of Flight-Secondary Ion Mass Spectrometry (ToF-SIMS). Org Geochem 2004;35(7):793–811; doi: 10.1016/j.orggeochem.2004.03.006.

van Kaam-Peters, H. M. E., Schouten, S., De Leeuw, J. W., & Sinninghe Damsté, J. S. A molecular and carbon isotope biogeochemical study of biomarkers and kerogen pyrolysates of the Kimmeridge Clay Facies: Palaeoenvironmental implications. Organic Geochemistry 1997;27:399–422.

Wickramasinghe RC, Pasterski MJ, Kenig F, et al. Femtosecond Laser Desorption Postionization MS vs ToF-SIMS Imaging for Uncovering Biomarkers Buried in Geological Samples. Anal Chem 2021;93(48):15949–15957; doi: 10.1021/acs.analchem.1c03275.

Wörmer L, Elvert M, Fuchser J, et al. Ultra-High-Resolution Paleoenvironmental Records via Direct Laser-Based Analysis of Lipid Biomarkers in Sediment Core Samples. Proc Natl Acad Sci U S A 2014;111(44):15669–15674; doi: 10.1073/pnas.1405237111.

Wörmer L, Gajendra N, Schubotz F, et al. A Micrometer-Scale Snapshot on Phototroph Spatial Distributions: Mass Spectrometry Imaging of Microbial Mats in Octopus Spring, Yellowstone National Park. Geobiology 2020;18(6):742–759; doi: 10.1111/gbi.12411.

FIGURES

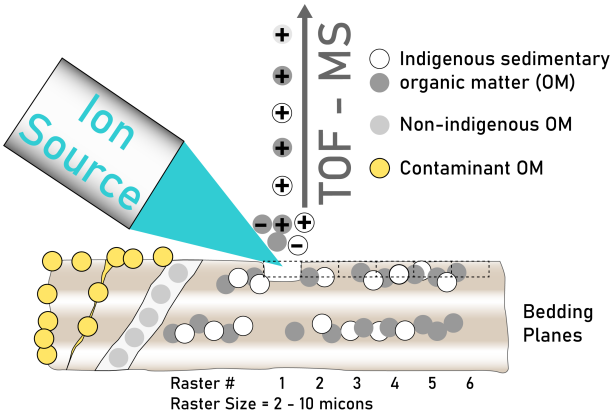

Figure 1. Schematic side view of a Mass Spectrometry (MS) imaging analysis and schematic cross section of a hypothetical sediment sample. Ionization of sample components depicted is occurring during desorption. Schematic representation of indigenous sedimentary organic matter (OM), concentrated in specific laminae, non-indigenous OM in material filling cracks, fissures and fluid inclusions, and contaminants on the sample exterior, open cracks and very near surfaces.

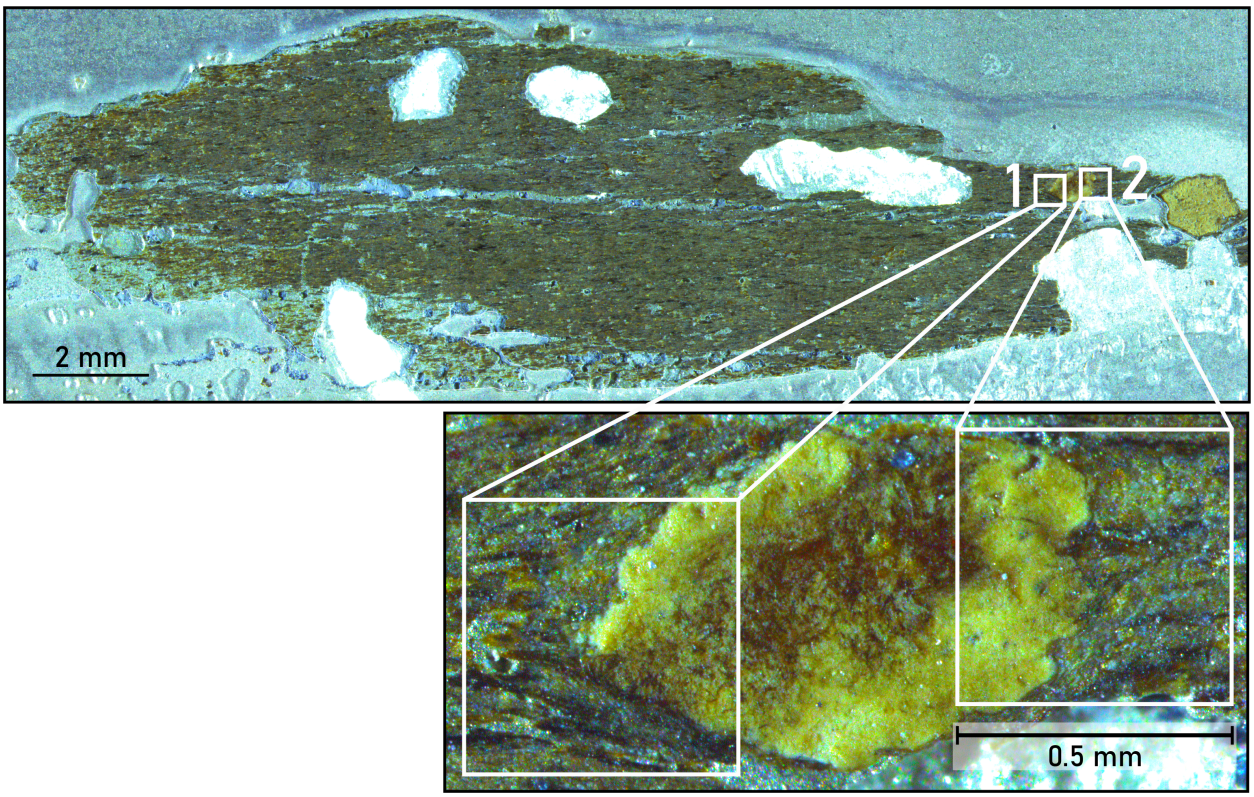

Figure 2. Optical micrograph of the Oxford clay thick-section of sample P89-13. White boxes indicate 500 µm × 500 µm regions analyzed via ToF-SIMS. The millimetric yellow grains are calcium phosphates.

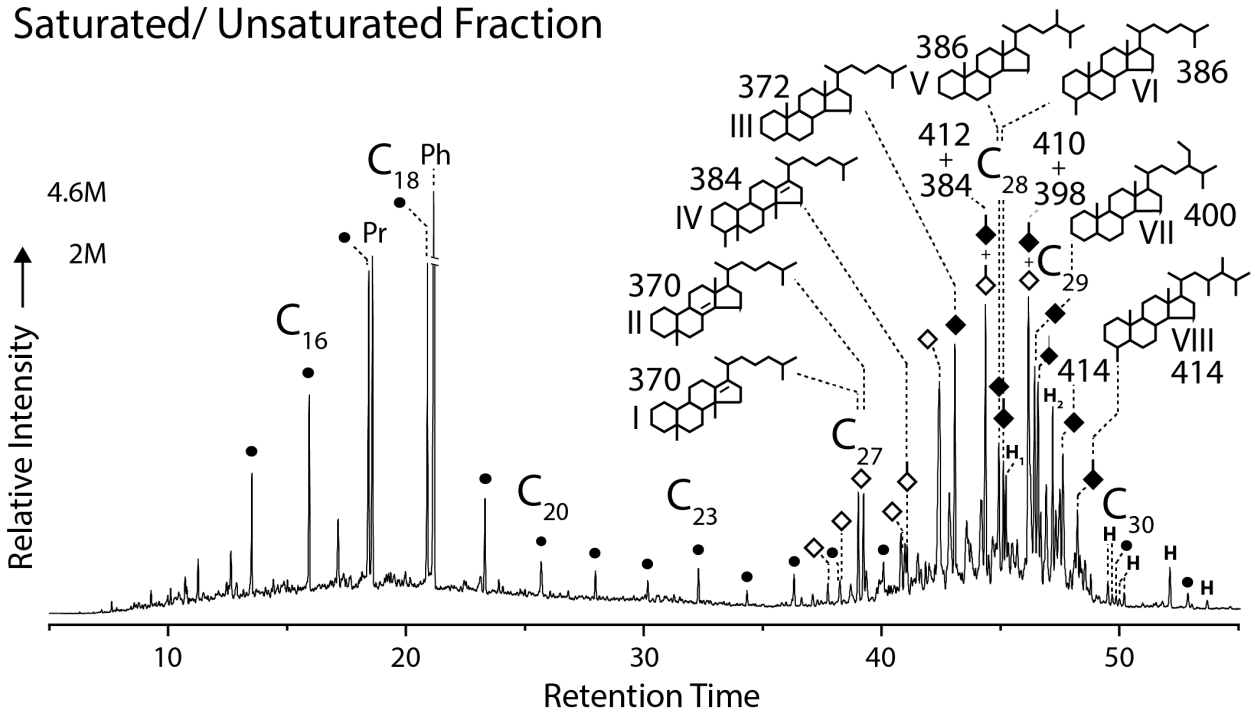

Figure 3. GC-MS total ion current (TIC) trace for the SUHF of sample P90-1. Peak assignments: Pr, pristane; Ph, phytane; ●, *n*-alkanes; ◇, sterenes and diasterene; ◆, steranes; ◇, unsaturated 4-methyl sterenes; ◆, saturated 4- and 24-methyl steranes; H, hopanes and hopenes, H_1 is C_{28} 22,30-bisnorhop-13(18)-ene, H_2 is C_{30} Hop-17(21)-ene; carbon number indicated for *n*-alkanes and steranes; molecular ion mass and structures indicated for select steranes and sterenes; Roman numerals next to structures correspond to compound names in Table 1.

Table 1. Molecular ions (M^+) and diagnostic fragment ions (Diag. EI ion, *m/z*) observed in the GC-MS data of the SUHF of sample P90-1, and potential peak identities (Potential ID) for each ion that may be observable within ToF-SIMS datasets. Roman numerals correspond to molecular structures shown in Fig. 3.

No. of C atoms	M^+ *m/z*	Potential ID – 1 (Diag. EI ion)	Potential ID – 2 (Diag. EI ion)	Potential ID – 3 (Diag. EI ion)	Potential ID – 4 (Diag. EI ion)
27	370	C_{27} – diasterene (**I**) (*m/z* 257)	Δ4, Δ5, Δ8(14) C_{27}-cholestene(**II**) (*m/z* 215)	spirosterenes (*m/z* 206)	
	372	C_{27} – cholestane (**III**) (*m/z* 217)			
28	384	4-methyl diasterenes (**IV**) (*m/z* 271)	4-methyl-cholestene (*m/z* 231)	24-methyl cholestene (*m/z* 215)	24-methyl spirosterenes (*m/z* 220)
	386	24-methyl-cholestane (**V**) (*m/z* 217)	4-methyl cholestane (**VI**) (*m/z* 231)		
29	398	24-ethyldiasterene (*m/z* 257)	4,24-dimethyl diasterene (*m/z* 271)		
	400	24-ethyl-cholestane (**VII**) (*m/z* 217)	4,24-dimethyl-cholestane (*m/z* 231)	4-desmethyl-dinosterane (*m/z* 217)	
30	412	4-methyl, 24-ethylcholestene (*m/z* 271)	C_{30} – diasterene (*m/z* 257)		
	414	4-methyl, 24-ethylcholestane (*m/z* 217)	C_{30} – diasterane (*m/z* 217)	Dinosterane (**VIII**) (*m/z* 231)	

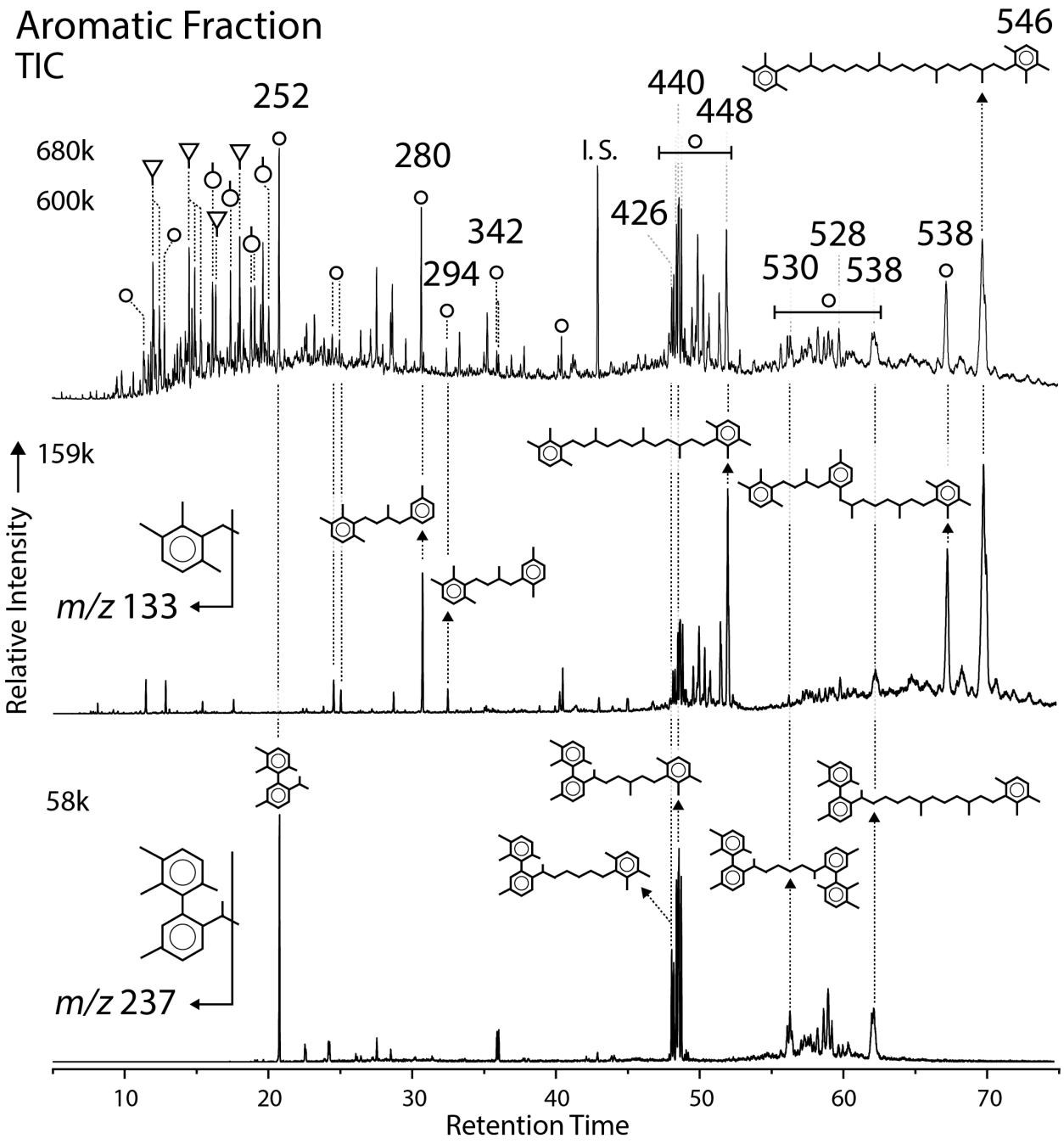

Figure 4. GC-MS TIC trace (top), mass chromatograms *m/z* 133 (middle) and mass chromatogram *m/z* 237 (bottom) for the aromatic fraction of sample P90-1. Peak assignments: ∇, methyl naphthalenes; ○, methyl biphenyls; ○, isorenieratene derivatives. Structures of isorenieratene derivatives are indicated with arrow s.

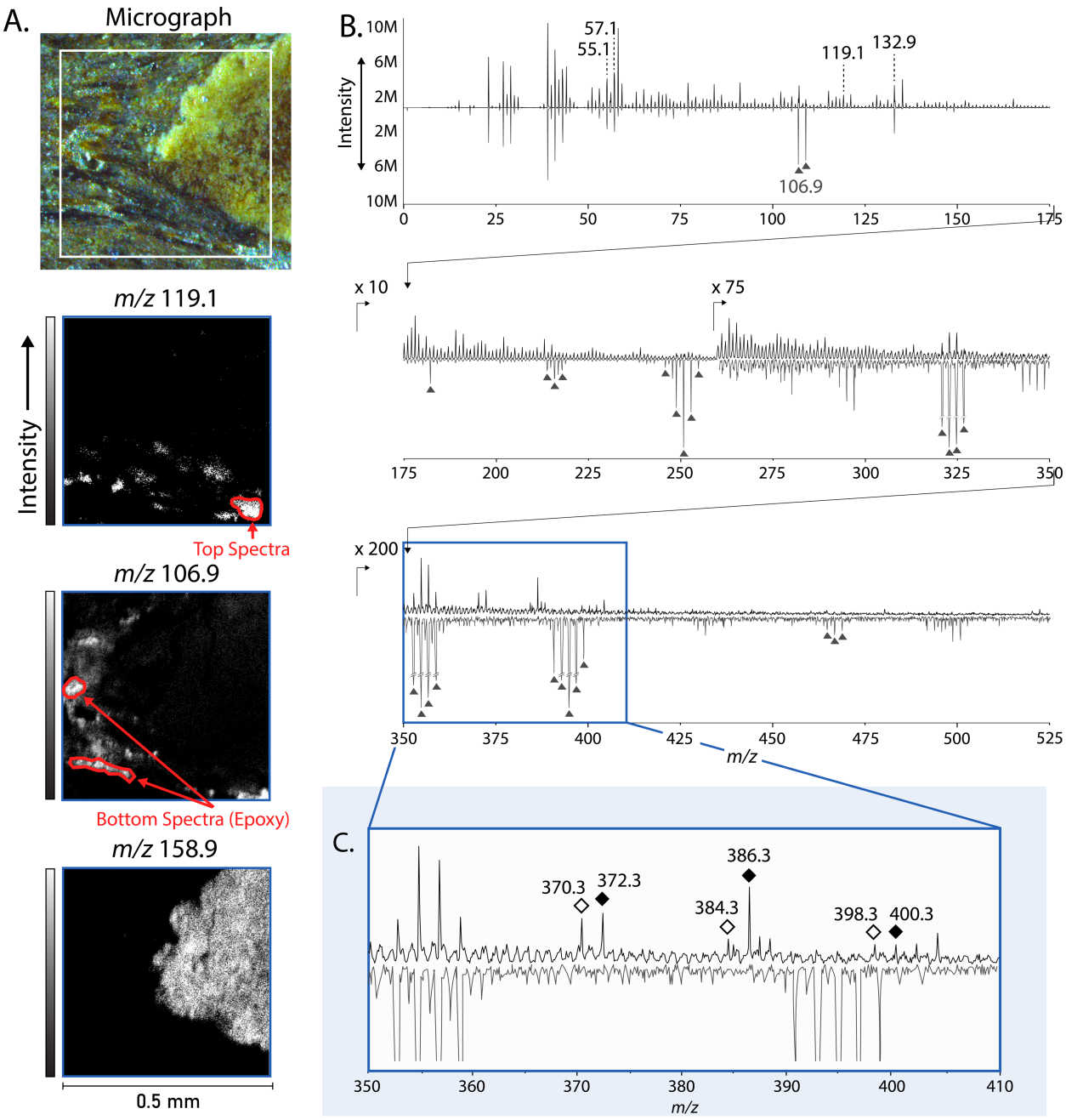

Figure 5. Analysis of Box 1 on sample P89-13 via ToF-SIMS and spectra extracted from specific regions of that sample. **A.** Photomicrograph (top) and ToF-SIMS MS maps **B.** Comparison of an average mass spectrum from the laminated region containing the fragment ion *m/z* 119.1 (top, black) and an average of mass spectrum obtained in an epoxy dominated area (bottom, grey). Triangles indicate Ag^+ ions. The spectra in B are average spectra obtained from the regions outlined in red in A. Labelled ions include classic organic fragment ions *m/z* 55.1 and *m/z* 57.1, fragment ion *m/z* 119.1 used to create the MS maps in A, and *m/z* 132.9 showing the presence of Cesium. **C.** Blown-up view of the ToF-SIMS spectra in B from *m/z* 350 to *m/z* 410 showing the occurrence of potential molecular ions of steroid hydrocarbons. Numbers indicate the exact masses of the ions.

Table 2. The *m/z* ratios and tentative peak assignments observed in spectra extracted from regions containing epoxy indicated within in Fig. 5.A. Peak assignments are suggested based on the distinct isotopic doublet of silver.

***m/z* of Observable Ions**	**Peak Assignment**
106.9, 108.9	Ag^+
213.8, 215.8, 217.8	Ag_2^+
214.9, 216.8, 218.8	Ag_2H^+
248.8, 250.8, 252.8	$Ag_2O_2H_3^+$
320.8, 322.8, 324.7, 326.8	Ag_3^+
352.7, 354.7, 356.7, 358.7	$Ag_3O_2H_3^+$
390.7, 392.7, 394.7, 396.7	$Ag_3O_4H_6^+$
534.6, 536.6, 538.6, 540.6, 542.6, 544.6	Ag_5^+
566.6, 568.6, 570.6, 572.6, 574.6, 576.6	$O_2Ag_5^+$
598.6, 600.6, 602.6, 604.6, 606.6, 608.6	$O_4Ag_5^+$

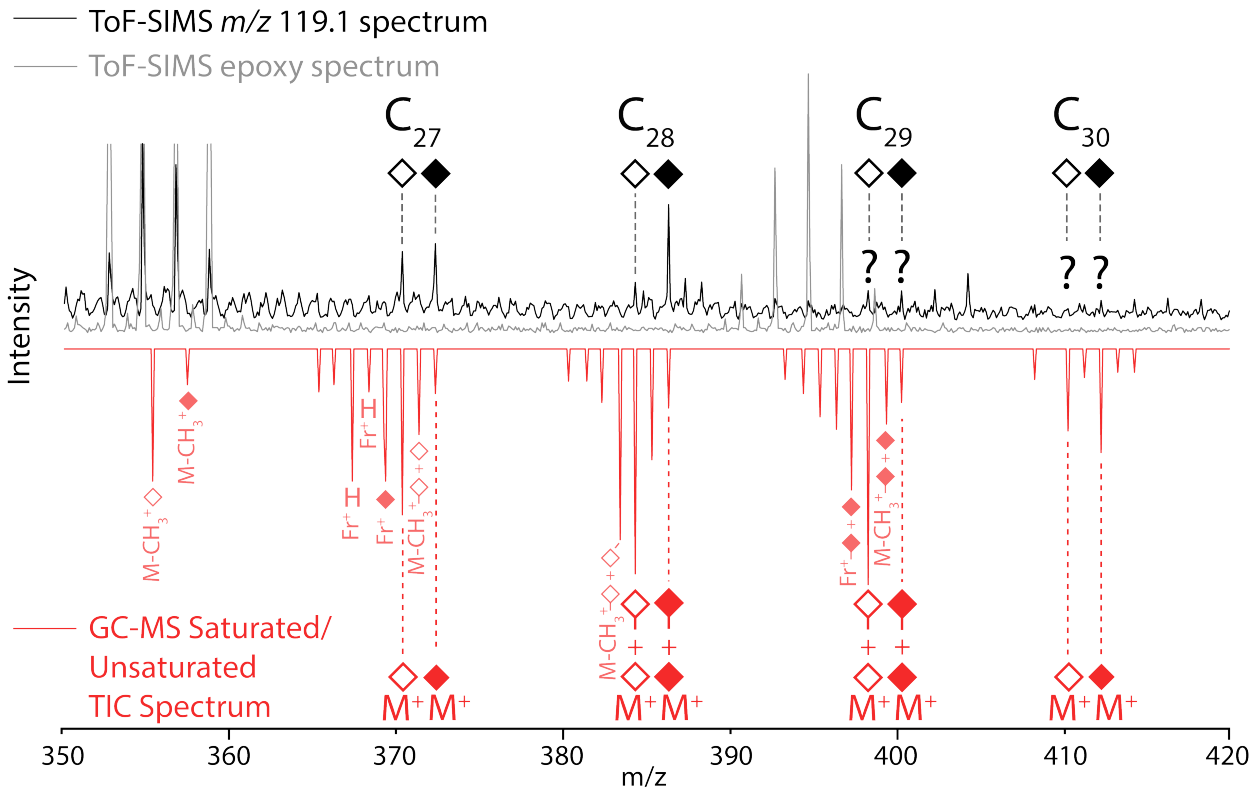

Figure 6. TOP. Partial ToF-SIMS average mass spectrum integrating regions with high *m/z* 119.1 signal (black) overlaid on an average mass spectrum integrating regions containing epoxy (grey) both obtained from the locations shown in Fig. 5.A. The labelling scheme follows that used in Fig 3. BOTTOM. Partial view of the GC-MS summed mass spectrum between 5 and 70 min, subtracted for background, for the SUHF of sample P90-1. M^+ indicates molecular ions, M-CH_3^+ indicates the molecular ions minus one methyl typically formed upon 70 eV EI of steroid hydrocarbons and Fr^+ indicates other fragment ions produced during 70 eV EI.

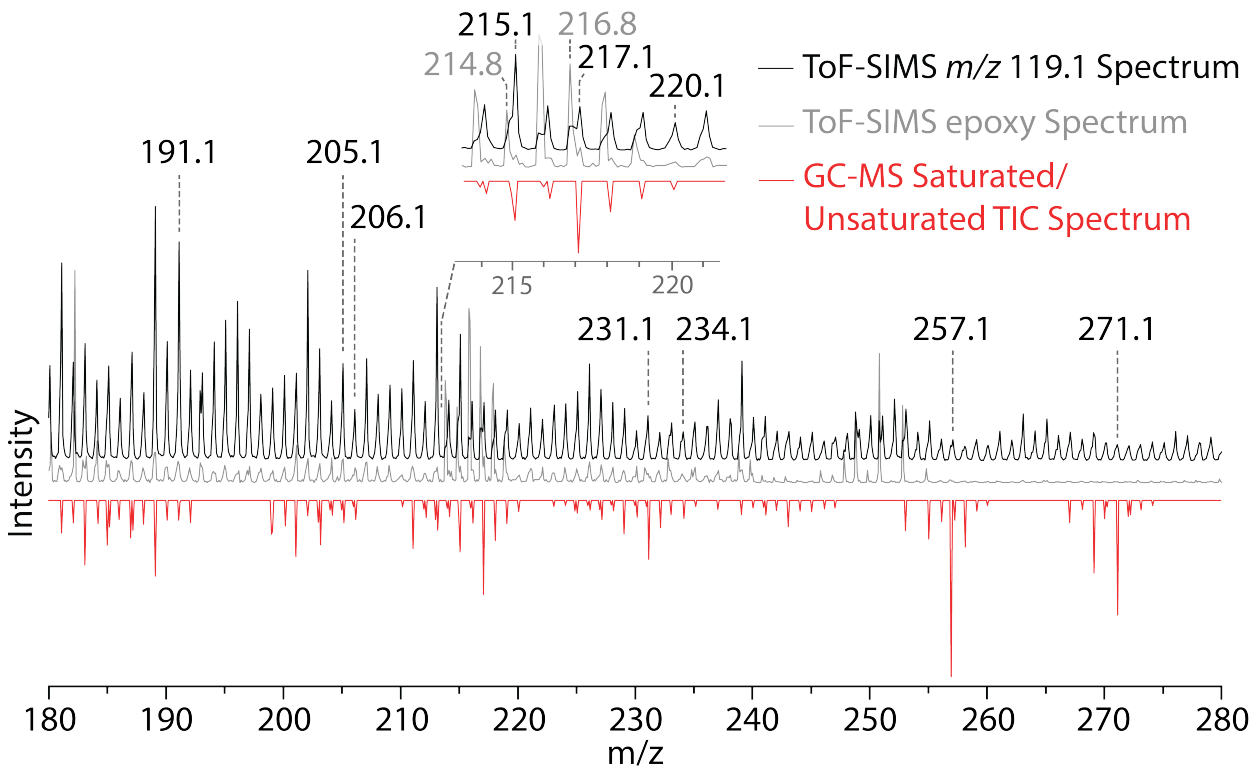

Figure 7. TOP. Partial ToF-SIMS average mass spectrum integrating regions with high *m/z* 119.1 signal (black) obtained from the locations shown in Fig. 5A overlaid on an average mass spectrum integrating regions containing epoxy (grey). Zoomed insets of spectra are chosen to highlight epoxy ions (Table 2) within the same mass range as potential sterane daughter ions *m/z* 215.1, *m/z* 217.1 and *m/z* 220.1. BOTTOM. Partial view of the integrated GC-MS mass spectrum between 5 and 70 minutes, subtracted for background, for the SUHF of sample P90-1.

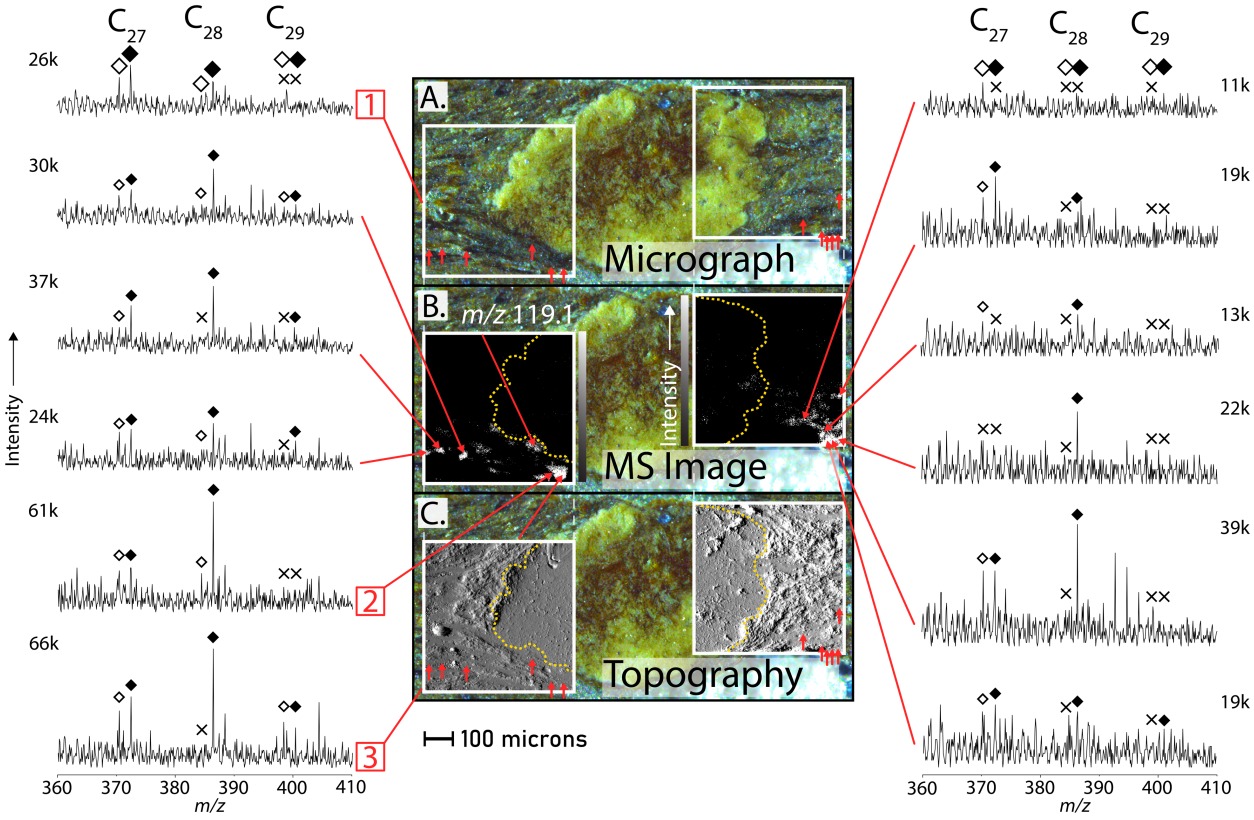

Figure 8. Optical micrograph (A), MS maps of *m/z* 119.1 (B), and SEM-BED-T topography images (C) of Boxes 1 and 2. Red arrows (A and C) and red lines (B) indicate the location of extracted ToF-SIMS point spectra (~50 pixels, total image area is 65,536 pixels). Yellow dotted lines on B and C indicate the location of the phosphate grain for reference. The phosphate grain boundary was defined using the MS map of *m/z* 158.9. Left and right are point spectra extracted from phosphate grain-flanking high *m/z* 119.1 regions. Closed diamonds indicate potential saturated steroid hydrocarbons, open diamonds indicate potential unsaturated steroid hydrocarbons, and potential carbon numbers are indicated above each ion. Spectra are scaled consistently within each box with values next to the spectra indicating the relative intensity of the maximum intensity ion within that spectrum. An 'x' indicates that the ion for the corresponding compound is below the limit of detection. Spectra 1, 2 and 3 have minimal (sub-micron) surface topography.

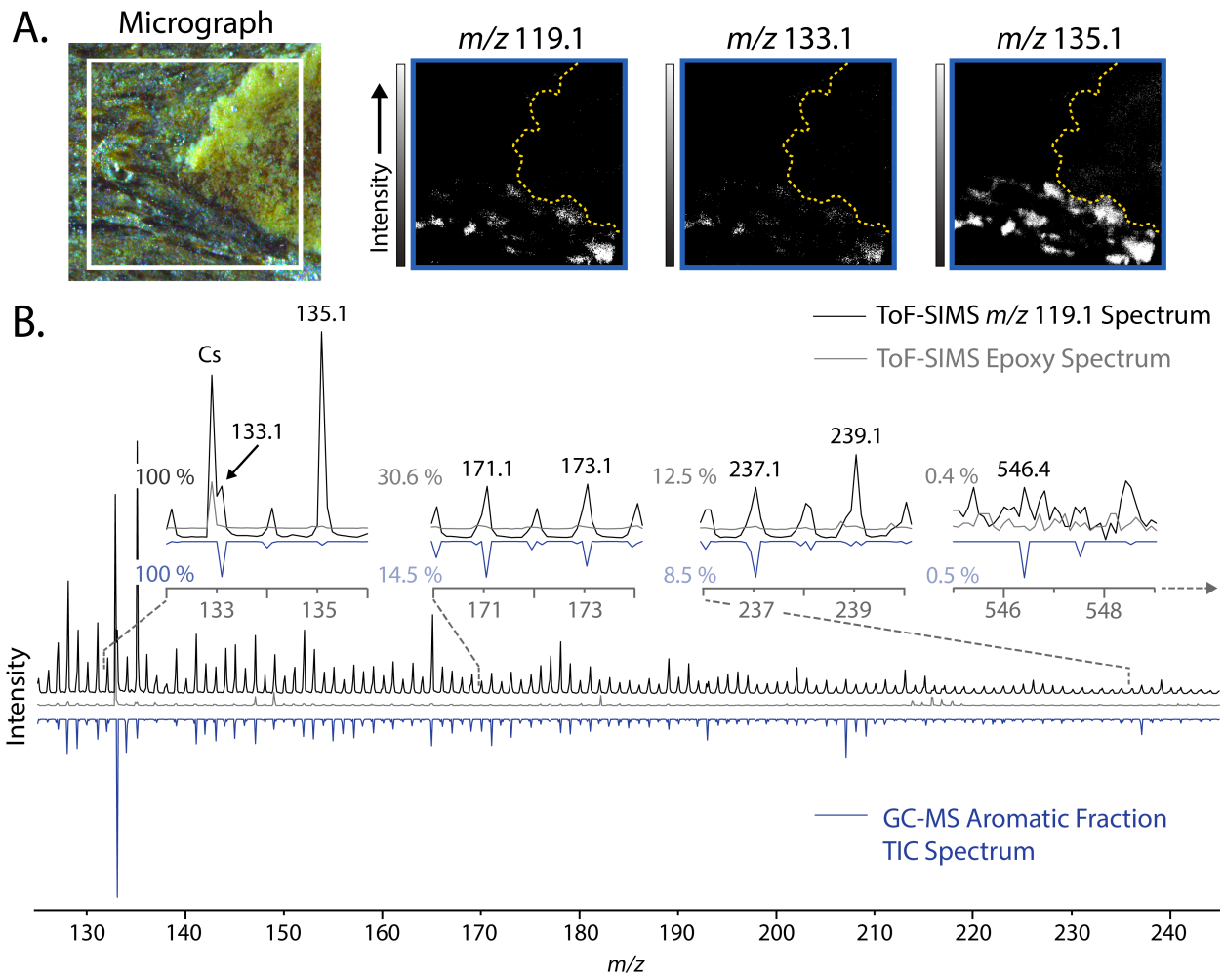

Figure 9. A. Photomicrograph and selected ToF-SIMS MS maps of fragment ion *m/z* 119.1, *m/z* 133.1 and *m/z* 135.1. A yellow dotted line indicates the location of the phosphate grain for reference, defined by the MS map of *m/z* 158.9 B. TOP. ToF-SIMS average mass spectrum integrating regions with high *m/z* 119.1 signal (black) in Fig. 5.A overlaid on an regional spectra epoxy (grey). Zoomed insets of spectra are chosen to highlight daughter ions of isorenieratene derivatives at *m/z* 133.1, *m/z* 171.1, and *m/z* 237.1, with the molecular ions of isorenieratane (*m/z* 546.4) outside of the mass range shown here. Inset labels include the intensity of the potential isorenieratene derivative daughter ions relative to *m/z* 133.1 expressed in percent and the exact mass of each daughter ion in the ToF-SIMS spectra. BOTTOM. Partial view of the integrated GC-MS mass spectrum between 5 and 70 min, subtracted for background, for the AHF of sample P90-1.